JOURNAL OF SOLID STATE CHEMISTRY **139,** 8–21 (1998)
ARTICLE NO. SC987773

Building up Complexity from Strips and Sheets: The Electronic Structure of the $La_{12}Mn_2Sb_{30}$ Alloy

Garegin Papoian and Roald Hoffmann[1]

Department of Chemistry and Materials Science Center, Cornell University, Ithaca, New York 14853–1301

Received September 26, 1997; in revised form February 2, 1998; accepted February 5, 1998

The bonding in the relatively complex $La_{12}Mn_2Sb_{30}$ alloy structure is analyzed with a retrotheoretical/building up process, implemented through a molecular orbital analysis of the various sublattices and the composite structure. In the antimony part of $La_{12}Mn_2Sb_{30}$ there are three relatively noninteracting networks: a three-dimensional Sb_{20} sublattice, an Sb_6 strip, and a one-dimensional array of isolated Sb atoms (of Sb_4 stoichiometry). A Zintl-type approach, modified for the clearly hypervalent nature of locally linear and square-planar Sb environments, leads to an initial partitioning of the electrons among the Sb sublattices; this electron counting eventually turns out to be in reasonable agreement with extended Hückel calculations. The electronic structure of the three-dimensional Sb_{20} sublattice in $La_{12}Mn_2Sb_{30}$ is derived theoretically from a two-dimensional square Sb sheet through first kinking the square sheet at every fifth diagonal line and then stacking the sheets, with Sb–Sb bond formation, into the third dimension. For the Sb_6 strips a second-order Peierls-type distortion of symmetrical vertex-sharing rhombi leads to the slightly asymmetrical strip structure observed. The *d*-block splitting of the Mn ions (in an unusual bicapped tetrahedral Sb environment) is described by a molecular model; arguments are given for localized bonding at Mn. There are significant La–Sb network interactions. The ability of the Sb networks in this structure to act as electron reservoirs is supported by our calculations.

A new series of ternary compounds with the general formula RE_6MSb_{15} (RE = La,Ce and M = Mn,Cu,Zn) were recently synthesized and characterized by Rogl, Cordier, and co-workers (1). All compounds in the series are isostructural, crystallizing in space group *Imm*2. Some of the alloys (Ce_6MnSb_{15} and Gd_6ZnSb_{15}) undergo antiferromagnetic ordering of the rare earth metal moments below 15 K, while the others remain paramagnetic down to 5K. The rare earth metals were found to be in oxidation state 3+ in all alloys, based on their magnetism. In the case of Ce_6MnSb_{15}, a high-spin $3d^5$ configuration was suggested for Mn from magnetic susceptibility measurements.

[1]To whom correspondence should be addressed.

Two views of the unit cell and the crystal structure of $La_{12}Mn_2Sb_{30}$ (there are two formula units per unit cell) are shown in Fig. 1. The structure is moderately complex and intriguing. There are six types of Sb atoms, labeled Sb4–Sb9. Atoms Sb4, Sb5, and Sb8 form two-dimensional kinked sheets (Fig. 2a), which can be derived from an idealized square sheet of Sb by folding at every fifth diagonal line. Square sheets of antimony are found in numerous rare earth antimony binary and ternary phases (2–10). These two-dimensional folded sheets are stacked into a three-dimensional Sb_{20} network (Fig. 2b) through Sb8–Sb8 bonds of length 2.88 Å. For comparison, a typical Sb–Sb single bond length (11) is 2.87 Å.

The next structural element perceived in these phases consists of one-dimensional strips (a "side" view, relative to Fig. 1, of one of these ribbons containing Sb7 and Sb9 is in **1**) of $(Mn_4)_{1/2}Sb_6 = Mn_2Sb_6$ stoichiometry. The Mn sites were reported to be half-occupied, which is the reason for writing the stoichiometry as we do. The Mn ions are surrounded by Sb in an approximate bicapped tetrahedral coordination, not a typical six-coordinate geometry.

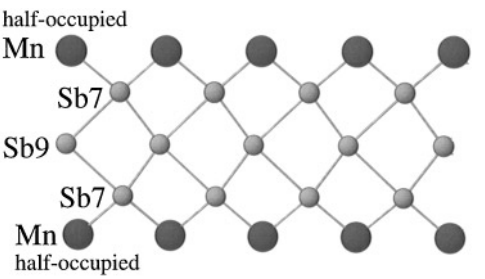

1

Finally, large channels present in the three-dimensional network of $(Sb_{20})(Mn_2Sb_6)$ (see Figs. 1b, 2b) are filled with one-dimensional arrays of La triangles at a distance of 4.31 Å between the triangles. The prismatic holes created by consecutive La triangles are occupied by Sb6 atoms. An analogous arrangement of Zr_3 triangles sandwiching Sb atoms was reported earlier (12). Putting all these substructures together, $La_{12}Mn_2Sb_{30}$ may be written as $(Sb_{20})\ (Mn_2Sb_6)(La_{12})(Sb_4)$.

0022-4596/98 $25.00

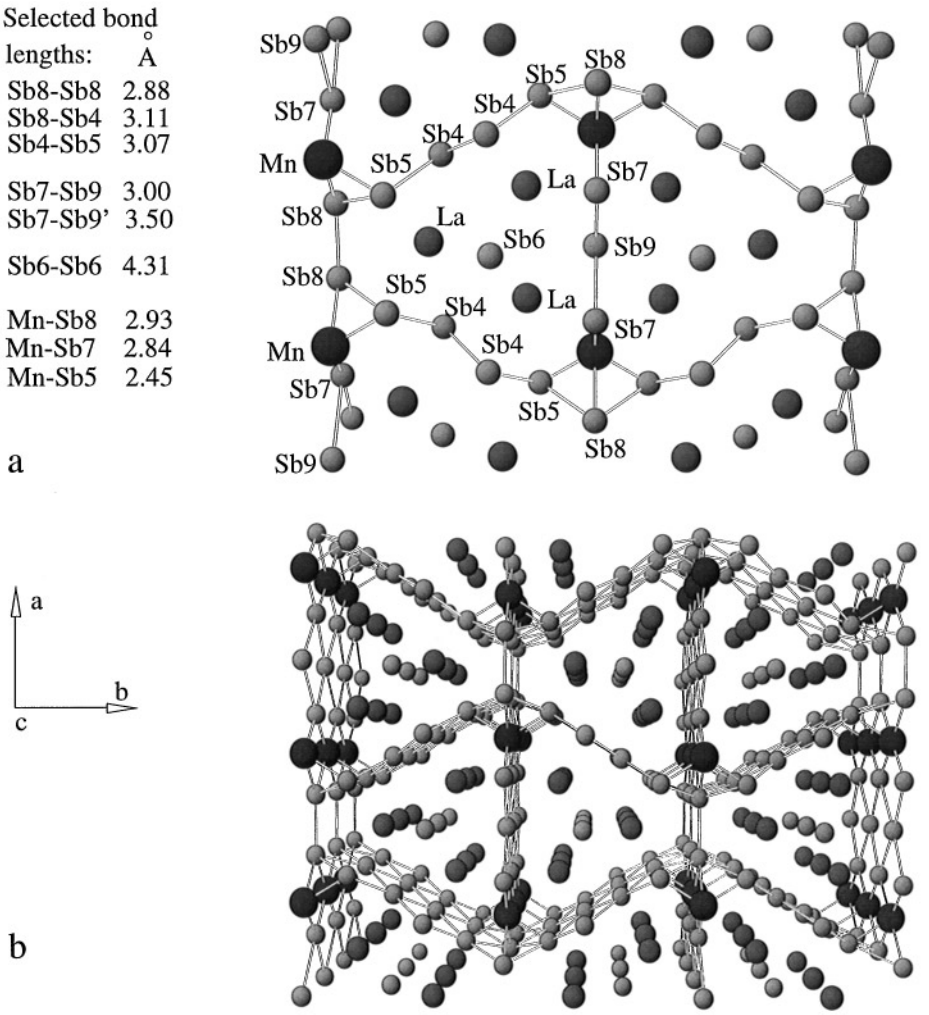

FIG. 1. (a) Unit cell of $La_{12}Mn_2Sb_{30}$. (b) Perspective view of the crystal structure of $La_{12}Mn_2Sb_{30}$: Sb, small spheres; La, medium size spheres; Mn, large dark spheres, half-occupied.

A RETROTHEORETICAL ANALYSIS

The variety of antimony substructures, vastly different in their dimensionality, attracted us to these molecules. In this paper we examine the electronic properties of $La_{12}Mn_2Sb_{30}$ by means of an approximate molecular orbital method, the extended Hückel theory (13–15). Our procedure is to decompose the crystal structure of $La_{12}Mn_2Sb_{30}$ into simpler substructures, independently analyze the latter, and then reassemble them to gain an understanding of the electronic structure of the alloy. Here is how this "retrotheoretical analysis" goes (Fig. 3).

First, the La atoms are removed from the alloy, followed by removal of Mn atoms. In the remaining Sb_{30} three-dimensional network there may be seen three relatively noninteracting substructures, namely, the three-dimensional Sb_{20} lattice (Fig. 2b), one-dimensional Sb_6 strips (see **1**, the Sb part only), and Sb_4 one-dimensional arrays of non-interacting Sb centers. Proceeding with the retrotheoretical analysis, we dissect the Sb_{20} substructure and then reconstruct it from two-dimensional kinked Sb sheets (Fig. 2a), which in turn may be derived from an idealized square lattice of Sb. At this point we reach a familiar entry point: the electronic properties of square lattices of main group elements that have been extensively studied (16). The one-dimensional Sb_6 strip (**1**, Sb part only) may be derived from an easily analyzed chain of vertex-sharing rhombi by a sliding motion of the central Sb9 atoms. We will also investigate the possibility of a Peierls-type sliding distortion (17) leading to the real strip geometry. The last (and simplest) Sb substructure is the one-dimensional array of widely separated (4.3 Å) Sb6 atoms.

At a first glance, our retrotheoretical approach may seem a convenient but abstract tool for analyzing the $La_{12}Mn_2Sb_{30}$ structure. But this is not so; the Sb substructures that are intermediate stages in the disassembly are closely related

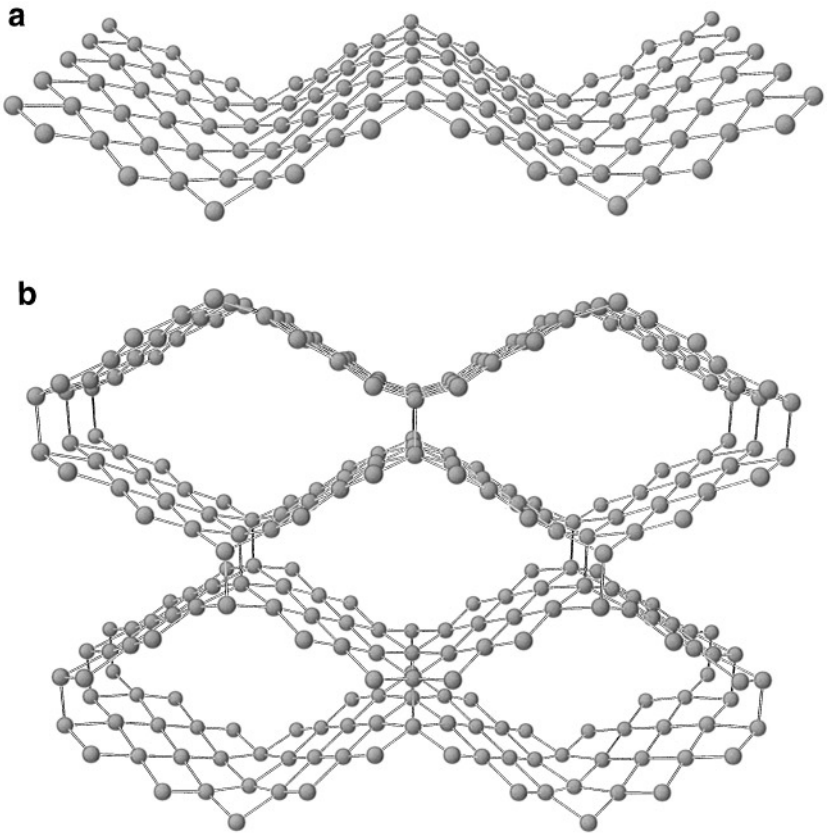

FIG. 2. (a) Two-dimensional kinked sheet of Sb. (b) Three-dimensional Sb_{20} substructure.

to real Sb substructures found in other compounds. We already mentioned the existence of square sheets of antimony in many rare earth metal antimony phases (2–10) and a one-dimensional chain of Zr_3 triangles with antimony atoms in the prismatic holes (12). Corbett and Garcia reported two undistorted Sb_3 strips connected sidewise in the α-$ZrSb_2$ structure (12). Linear isolated Sb_3 fragments were found in $Eu_{14}MnSb_{11}$ (18). The bonding in the $La_{12}Mn_2Sb_{30}$ substructures sheds light on similar Sb substructures found in other compounds and provides an entry point for a forthcoming general comparative study of Sb substructures in rare earth metal antimony binary and ternary phases.

ELECTRON COUNTING IN THE ANTIMONY SUBSTRUCTURES

What charges might one assign to different substructures of $La_{12}Mn_2Sb_{30}$? This material is an alloy and the electronegativities of the elements involved are not very different from each other. On the other hand, magnetic measurements indicate classical formal charges for rare earth metals and Mn(1). Therefore, we are led to a Zintl-type approach in assigning the charges to different Sb substructures. Twelve tripositive La atoms would contribute 36 electrons to the Sb sublattice. Two Mn atoms were found to be in the $2+$ oxidation state for the Ce analog of our compound. If we presume the same degree of formal electron transfer in $La_{12}Mn_2Sb_{30}$, the Sb subnetwork should be formally written as Sb_{30}^{40-}.

The difficult task is to divide the $40-$ charge among the three Sb substructures. The Sb6 atoms in the Sb_4 chain are well isolated from each other and, therefore, may be confidently assigned a formal $3-$ charge to complete octets around them (for a total of $12-$ per unit cell). After this things become less obvious.

The one-dimensional Sb_6 strips are constructed from side and central Sb atoms with presumably different electron counts. Since the central atoms of the strips are nearly square-planar, we are led to make an analogy to known, hypervalent, late main-group compounds. To derive a reasonable electron count for the strip, we start first from the molecular hypervalent square-planar XeF_4 (**2**). The bonding in this molecule is pretty well understood in terms of electron-rich three-center bonding (19). In a hypothetical dimer, derived from XeF_4 by sharing vertices, one has to replace bridging fluorines with oxygens if one wants to preserve the same electron count (formally Xe^{4+}, **3**). Continuing this line

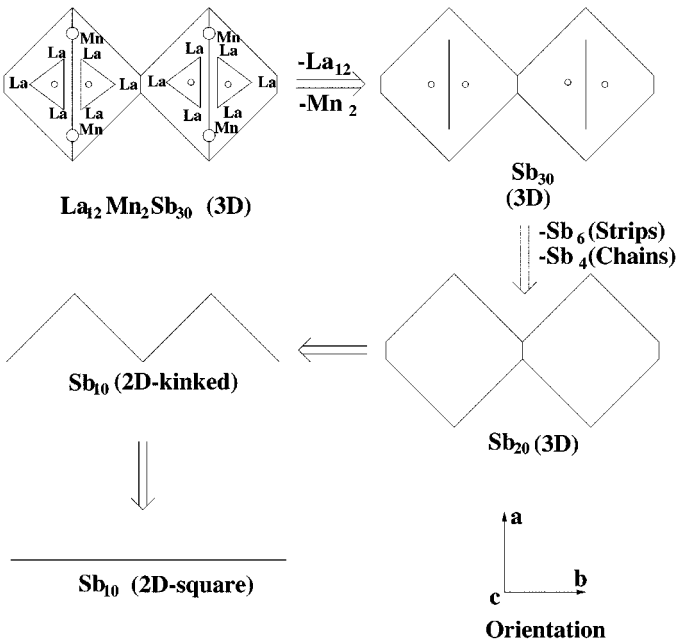

FIG. 3. Schematic representation of "retrotheoretical" disassembly of $La_{12}Mn_2Sb_{30}$. A side view parallel to the *c* axis is shown.

of reasoning, a very hypothetical polymer of XeO_2 stoichiometry (**4**) should have a bonding pattern similar to the original XeF_4 molecule (two three-center four-electron bonds in the plane, plus two lone pairs per Xe). We assume, just as a starting point, that the Sb_3 strip is isoelectronic to the hypothetical XeO_2 polymer. This suggests a $1-$ charge on the side Sb atoms and a $3-$ charge on the central Sb atoms (Sb_3^{5-}) (**5**). Since there are two repeat units of the strips in the unit cell of $La_{12}Mn_2Sb_{30}$, the strips are postulated (at this simplistic stage, before detailed calculations) to carry 10 negative charges per unit cell (Sb_6^{10-}).

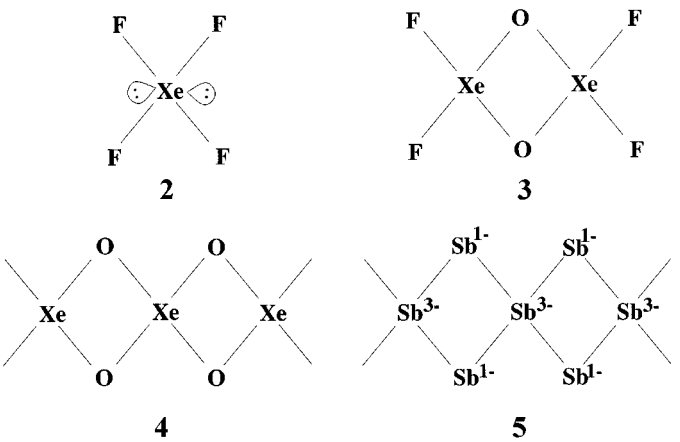

Linkage of the (still very hypothetical) one-dimensional XeO_2 polymers (**4**) by sharing the remaining vertices will produce a two-dimensional square sheet (**6**). One has to replace doubly connected oxygen atoms by quadruply connected carbon atoms in order to preserve the electron count at Xe of Xe^{4+}. There are then on the average $(8 + 4)/2 = 6$ electrons per site in the hypothetical XeC square sheet (20), which corresponds to a $1-$ charge per Sb for the analogous Sb square sheet. Note that, as in XeF_4, this electron count implies two lone pairs on each Sb atom (equivalent to *ns* and np_z orbitals). Jeitschko and co-workers, based on their experimental results, assigned one electron per long Sb–Sb bond in the Sb substructures, which also led them to a $1-$ charge on Sb in the square sheet (9, 21). The overall charge for the unit cell stoichiometry is Sb_{20}^{20-}. Kinking of the square sheet at every fifth diagonal line does not change the electron count for the system.

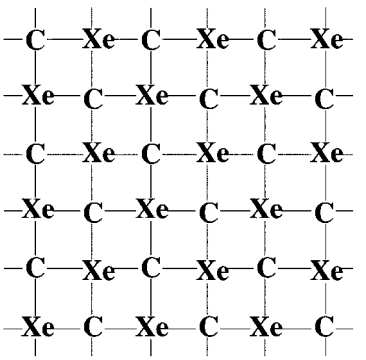

To form a bond between the sheets, as is observed, requires oxidation. Structure **7** illustrates this; one cannot form a bond between two lone pairs (at the hypervalent antimony atoms of the kinked sheet), but needs to remove one electron per Sb. For the sheet this requires removal of one-fifth of the negative charge of Sb_{20}^{20-}.

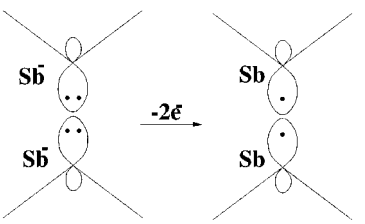

The reasoning pursued here, the hypervalent extension of the Zintl concept, leads to a $16-$ charge on the Sb_{20} substructure. The total charge on the Sb_{30} subnetwork becomes $38-$, 2 electrons short of the required $40-$. Two electrons out of a total of 200 electrons in the unit cell is not much. So perhaps with a little reduction, the electron counts derived above might serve as reasonable starting point. Another viewpoint is that we might as well see what

computations give for charges on the various sublattices. One of the referees pointed out that the Mn occupancy in the experimental study may not have been refined, so there might be some transition metal nonstoichiometry, altering the electron count (22). Perhaps the extended Zintl count is not unrealistic.

HOW TO JUDGE WHETHER AN Sb–Sb BOND IS PRESENT

Throughout this paper we are faced with making judgments whether an Sb–Sb bond is present and, if so, how strong it is. This is a theoretical question with no unambiguous answer. A calibration is in order. We approach it by calculating a measure of bond strength, the Mulliken overlap population (23), as a function of distance for some diatomic molecular systems. Quite unambiguously there is no Sb–Sb bond in Sb^{3-} interacting with Sb^{3-} (isoelectronic to a Kr–Kr interaction); there should be a single bond in Sb_2^{4-} (isoelectronic to Br–Br); and a double bond in Sb_2^{2-} (as in O_2); and a triple bond in the Sb_2 molecule analogous to N_2. Figure 4 shows computed Sb–Sb overlap populations as a function of separation; note how they differ. As we encounter overlap populations values calculated for various Sb–Sb bonds in the $La_{12}Mn_2Sb_{30}$ structure, we use these calibration curves as standards for estimating bond multiplicity.

THE SQUARE-PLANAR Sb

Consider the band structure (Fig. 5c) of a square sheet of Sb, located in the xy plane with an Sb–Sb separation of 3.08 Å, an average of those in the sheet (Fig. 5b). The Fermi level is tentatively specified at that for Sb^{1-} for reasons given above. A qualitative discussion of the bands for a square lattice may be found in a book by one of us (24). The crystal orbitals at different symmetry points are drawn in Fig. 6. The p_z band (z is perpendicular to sheet) does not mix by symmetry with other bands for any k in the reciprocal space. It is contained within the -13 to -8-eV energy window and is fully occupied for this Sb^{1-} electron count, as expected from our comparison to hypervalent XeF_4 (the p_z orbital is the Xe lone pair combination higher in energy). The p_x and p_y bands are doubly degenerate at Brillouin zone special points Γ and M and are not allowed to interact by symmetry with the s band at those points. At Γ, the zone center, the p_x and p_y bands are σ antibonding and π bonding (24); they are therefore higher in energy than the σ-bonding s band.

Along the Γ–X symmetry line, the degeneracy of p_x and p_y bands is broken and the p_x and s bands are allowed to mix by symmetry. At X, the p_x band is σ and π bonding and lies significantly lower in energy than the p_y band, which is σ and π antibonding. Of course, from Γ to Y the results are analogous, with the roles of p_x and p_y reversed. The band structure along the Γ-to-M symmetry line is little more complicated. It is convenient to define new basis functions p_+ and p_-, the sum and the difference of the original p_x and p_y. The p_+ band belongs to the same irreducible representation as the s band along the Γ-to-M line and these two bands mix with each other. The p_- band remains orthogonal to all other bands along that particular symmetry line. The s, p_x and p_y, and p_z contributions to the total density of states (DOS) (25) of the Sb^{1-} square sheet confirm the expected dispersions of these bands (only the p_z contribution is shown in Fig. 5d).

The crystal orbital overlap population (COOP, an energy-resolved overlap population) (25) curve between neighboring Sb atoms is shown in Fig. 5e. Some Sb–Sb antibonding states are populated for the electron count specified for the sheet, lowering the total overlap population from the maximum of 0.42 (for 4 electrons per Sb) to 0.23 (for 6 electrons per Sb, Sb^{1-}). This overlap population is less than half of the overlap population of 0.5 calculated for the hypothetical Sb_2^{4-} molecule with a presumably single Sb–Sb bond at the corresponding distance of 3.08 Å (see Fig. 4). This reduction of the bond strength is characteristic of the hypervalent nature of Sb atoms. Our results are in qualitative agreement with the experimental work of Jeitschko and co-workers (9, 21), who assigned a bond order of a half to the longer Sb–Sb contacts in antimony subnetworks, including the Sb square sheet.

The antibonding orbitals that lower the Sb–Sb OP from its maximum value are the upper part of the p_z band, as well as the middle of the $\{s, p_x, p_y\}$ bands, which are not nonbonding, but actually antibonding, as indicated

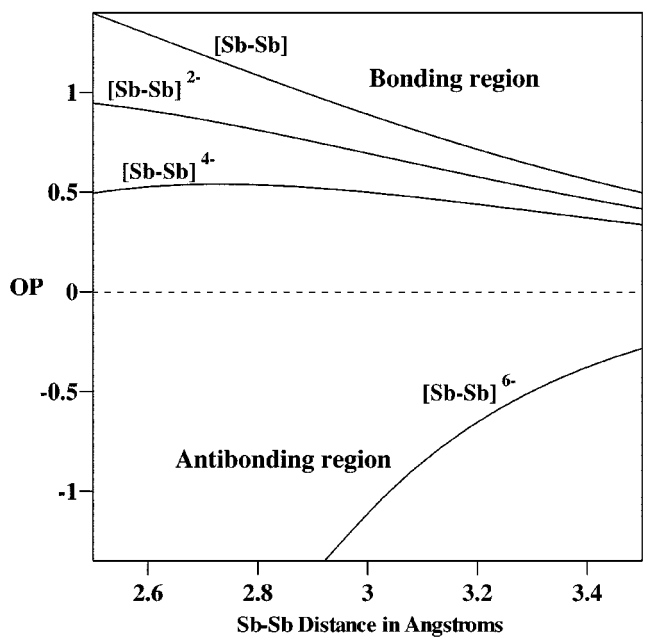

FIG. 4. Overlap population (OP) curves for Sb_2^{6-}, Sb_2^{4-}, Sb_2^{2-}, and Sb_2.

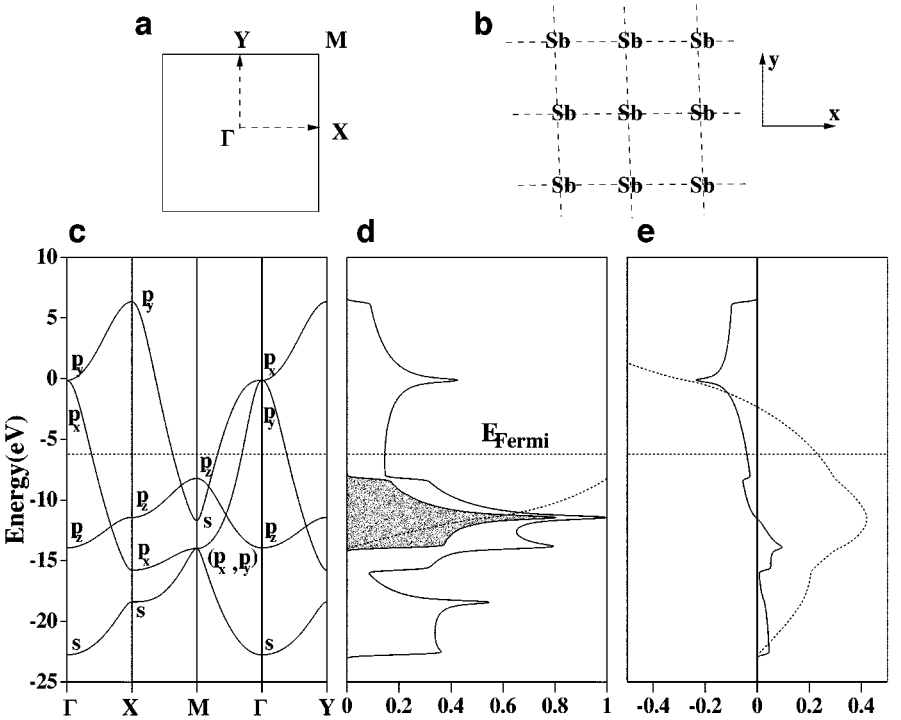

FIG. 5. (a) Brillouin zone. (b) Square sheet of Sb. (c) Band structure of the Sb^{1-} square sheet. (d) p_z contribution to the total DOS. (e) Sb–Sb COOP (solid line) and its integration curve for the interaction between neighboring atoms (dotted line).

schematically for a one-dimensional chain cut out from the sheet in **8**. Thus, oxidation of the sheet (from Sb^{1-}) would strengthen bonds between Sb atoms. One has to be cautious here; too much oxidation of the sheet would lead to a neutral Sb net, which would prefer to be three- rather than four-connected.

8

KINKING THE SQUARE SHEET OF Sb^{1-} AND STACKING THE SHEETS INTO A THREE-DIMENSIONAL NETWORK

We next calculated the electronic structure of the two-dimensional (2D) kinked Sb sheet (Fig. 2a) with the Sb–Sb distances taken from the original crystal structure of $La_{12}Mn_2Sb_{30}$. The sheet is then slightly distorted from the hypothetical geometry of a 2D square Sb sheet derived by kinking the idealized square Sb network at every fifth diagonal line.

The Sb4, Sb5, and Sb8 atom contributions to the total DOS of the kinked Sb sheet were compared with the corresponding contributions with the total DOS of the perfect square Sb sheet to gauge the degree of perturbation of the square sheet. Sb8 is the sheet atom that forms an intersheet bond (see Fig. 1); the superposition of the integrated DOS projections (not shown here) indicated that the effect of the perturbation indeed is noticeable only for the corner Sb8 atoms.

The most interesting consequence of kinking of the square Sb sheet is the formation of relatively localized lone pairs on the corner Sb8 atoms, with attendant s–p_z hybridization. The creation of directional lone pairs on pyramidalization of square-planar molecules is well described elsewhere (26). For example, a little of that s–p_z mixing may be seen in crystal orbital 14 at Γ (Fig. 7). Note that this orbital also has substantial Sb5 character. There are three more crystal orbitals at Γ with analogous directionality. These orbitals are well prepared for interaction with each other on stacking of two-dimensional sheets into a three-dimensional network; Fig. 8a shows the contributions of p_z orbitals to the total DOS. Localization in energy is equivalent to localization in real space (27). We are going to explore this stacking of the sheets next.

So far we have lone pairs (p_z) perpendicular to the kinked sheet. If two such sheets are brought together, the interaction of the filled lone pairs will be repulsive, as we argued above (structure **7**). One has to remove one electron from each corner Sb p_z orbital to allow bond formation. What is happening is nothing unusual; the molecular equivalent would be repulsion between two approaching Sb^{3-} ions,

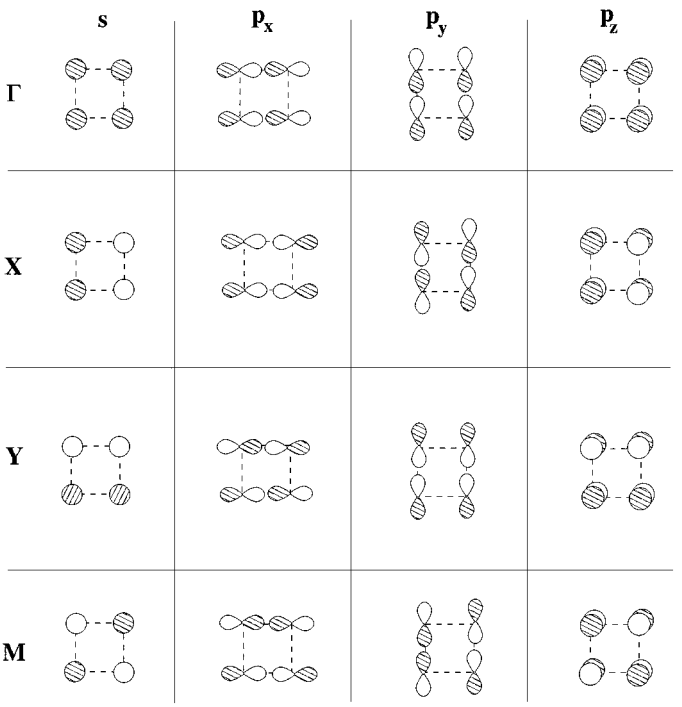

FIG. 6. Crystal orbitals of the Sb^{1-} square sheet at Γ, *X*, *Y*, and *M*. Only four unit cells are shown.

changed to an attractive interaction, the formation of a σ bond, on oxidation of each to Sb^{2-} (see **7**). Of 20 atoms in Sb_{20}^{20-}, only 4 are corner Sb8 atoms; therefore, the removal of 4 electrons will reduce the charge to 16−. Figure (8) b shows clearly the Sb8–Sb8 bonding (σ) and antibonding (σ^*) state regions in the DOS of the composite 3D network, split significantly up and down from the lone pair contribution in a single kinked sheet in Fig. 8a. We see here the extended structure equivalent of simple single bond formation, as shown schematically in **9**.

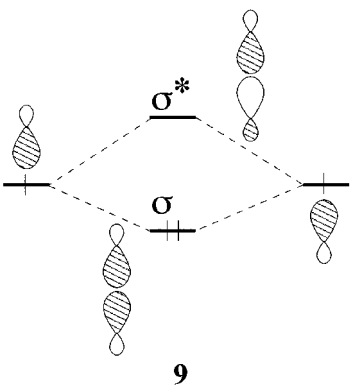

9

Compared with kinking, the assembly of the Sb_{20} three-dimensional substructure (Fig. 2b) from the 2D sheets (Fig. 2a) is a significantly stronger perturbation, just because of

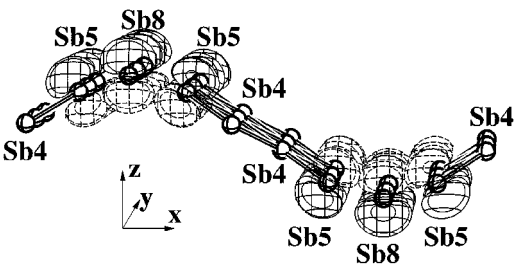

FIG. 7. Crystal orbital No. 14 of the kinked Sb sheet at Γ.

the bond formation between the sheets. We also probed the degree of bond localization within the Sb network. One good indication of a localized bond is the degree of conservation of the bond's COOP curve when a perturbation is applied somewhere else in the system: the smaller the change, the more localized the bond. We found that, although immediately adjacent to the interacting Sb8 atoms, even the Sb8–Sb5 bond COOP is not altered on stacking; we therefore argue that bonding in the sheets is essentially localized. The intersheet overlap population between Sb8 atoms (0.63) is significantly higher than various intrasheet overlap populations between Sb atoms (around 0.25). The Sb8–Sb8 overlap population is comparable to a single-bond Sb–Sb overlap population in Sb_2^{4-} (Fig. 4).

The Fermi level passes through the antibonding region of the intrasheet COOPs in the 3D Sb_{20}^{16-} network, but in a COOP region that is Sb8–Sb8 nonbonding (Fig. 9). Therefore, possible oxidation of the substructure would strengthen the *intra*-sheet Sb–Sb bonds but leave *inter*sheet bonding unaffected.

We may summarize the preceding two sections as follows: directional orbitals are created by kinking the square sheet of Sb. These orbitals are well suited for interaction with each other on stacking. The bonding in the sheets is strongly localized; some oxidation should strengthen bonding in the system.

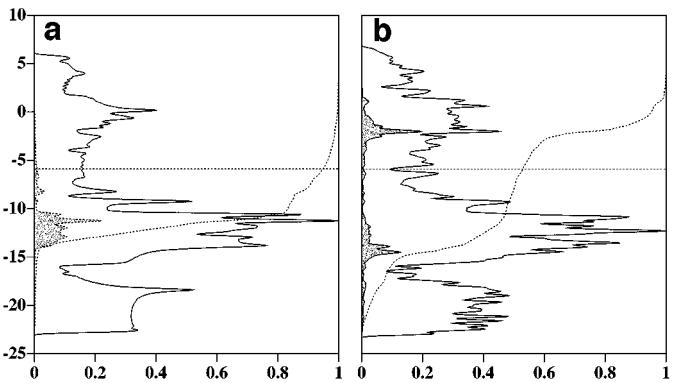

FIG. 8. p_z orbital contribution to the total DOS of (a) 2D kinked Sb sheet and (b) 3D Sb network.

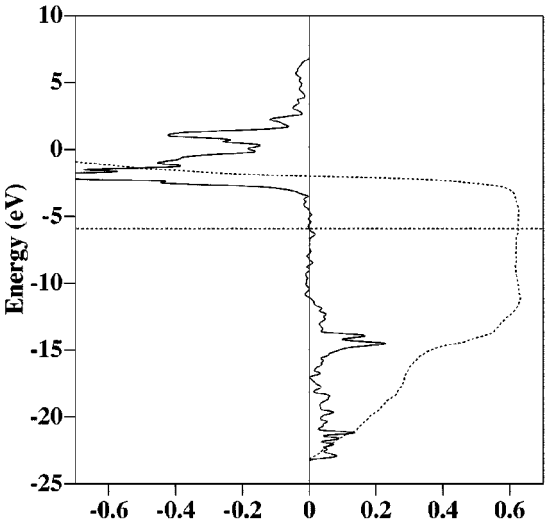

FIG. 9. Sb8–Sb8 COOP (solid line) and its integration (dotted line) in 3D Sb_{20}^{16-}; the horizontal dotted line indicates the Fermi level for Sb_{20}^{16-}.

Sb_3 ONE-DIMENSIONAL STRIPS

The second substructure of the Sb network consists of one-dimensional Sb_3 strips **10**. The central Sb9 atoms in the chains are located somewhat asymmetrically with respect to the side Sb7 atoms. The short Sb9–Sb7 distance is 3.00 Å and the long one is 3.50 Å.

A more symmetrical structure **11** (which we shall call idealized) may be related to the observed structure by a collective sliding motion of the central Sb9 atoms (shown exaggerated, in **11**, with arrows). In the idealized strip the central Sb9–side Sb7 distance is taken as 3.23 Å, the mean of the two real distances. It is quite natural to ask whether the real structure is related to the symmetrical structure through a Peierls-type sliding distortion, and this is the question we examine next.

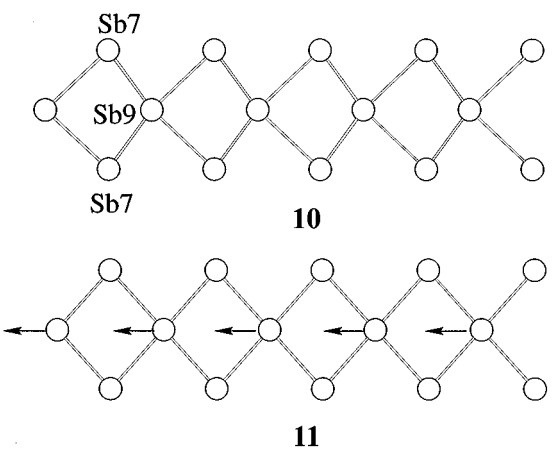

The band structure of the symmetrical Sb_3^{5-} strip, a chain of vertex-sharing Sb rhombi (Sb7–Sb9–Sb7 angle 96°), is shown in Fig. 10a. The Fermi level is calculated for a 5− charge per Sb_3 unit, as discussed in the Introduction.

We analyze next the sliding motion of the central Sb atoms in the idealized Sb_3 strip. The main consequence of such a sliding is the loss of the symmetry plane perpendicular to the polymer (x) axis. This results in mixing of the bands that were not allowed to interact at Γ and X. This effect is important for the highest filled and lowest unfilled bands, Nos. 10 and 11. Bands 10 and 11 of the idealized chain repel each other strongly on sliding, forming bands which are less and more antibonding bands, respectively (Fig. 11). The interaction is strongest at Γ because of the small energy difference between these bands (see Fig. 10b).

Band 10, occupied by two electrons, contributes 1.24 eV to the total stabilization of 1.31 eV on sliding, indicating that the interaction of bands 10 and 11 plays by far the dominant energetic role in the distortion. This kind of interaction of filled and unfilled bands, leading to a distortion, is the solid-state analog of a second-order Jahn–Teller distortion (28). We also carried out calculations on a corresponding distortion of the strips in the full crystal structure of $La_{12}Mn_2Sb_{30}$. The distorted (real) structure is still favored over the idealized one by 0.8 eV.

The positions of the side Sb7 atoms of the ribbon may be imagined fixed by Mn and La in the crystal structure of $La_{12}Mn_2Sb_{30}$. The central Sb atoms can move relatively easily only in the plane of the strips, their "out-of-plane" motions being restricted by the La atoms. Keeping this in mind, we calculated in addition to the sliding motion (structure **11** and Fig. 12a) three other possible motions of the central atoms: a pairing motion (Fig. 12b), all central Sb atoms sliding "up" in the y direction (Fig. 12c), and the central Sb atoms moving alternately up and down in the

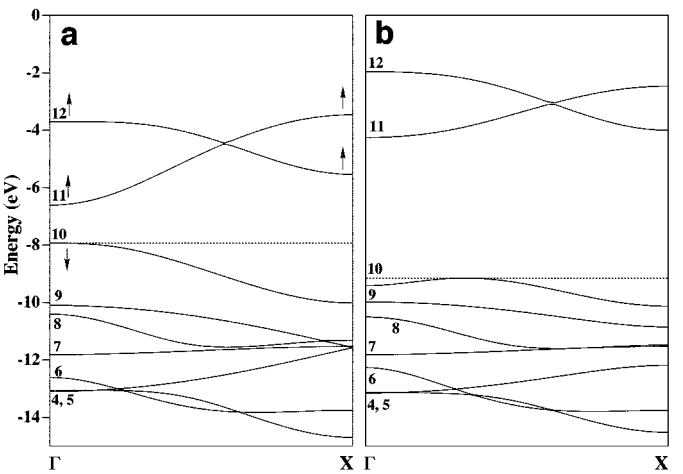

FIG. 10. Comparison of the band structures of the idealized (a) and the real (b) Sb_3^{5-}. The movement in energy of important bands on distortion is indicated by arrows.

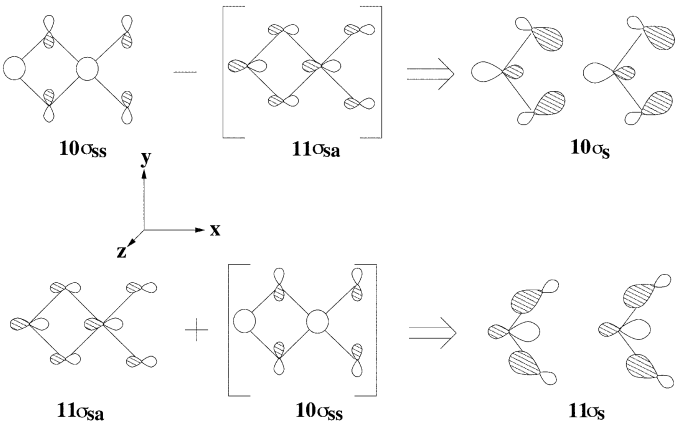

FIG. 11. Interaction of crystal orbitals 10 and 11 at Γ in the sliding distortion. The first symmetry label refers to orbitals symmetric and antisymmetric with respect to the *xz* plane; the second, with respect to the *yz* plane. The distortion removes the second plane.

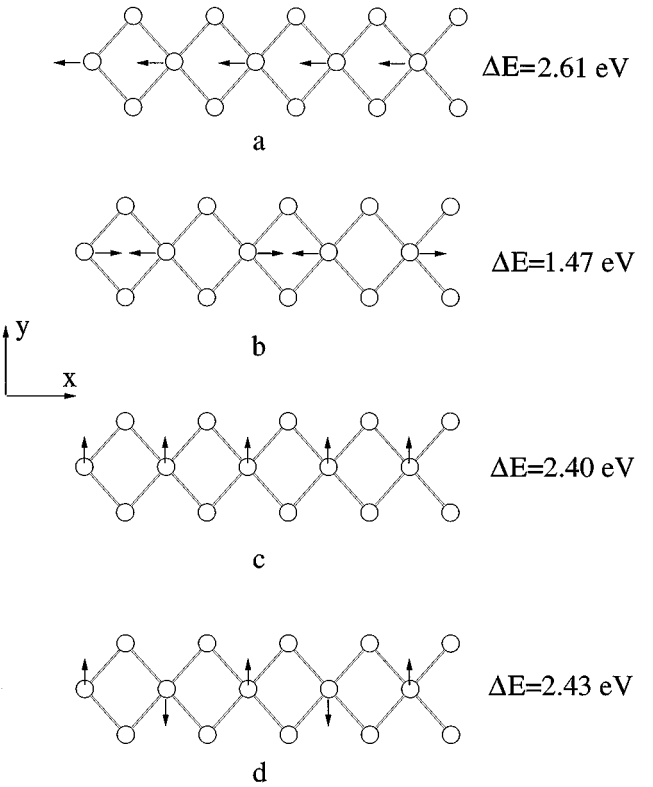

FIG. 12. Different distortions of the central Sb atoms in the doubled unit cell: (a) sliding distortion, (b) pairing distortion, (c) all-up distortion, (d) up-down distortions. ΔE indicates the total energy gain per two unit cells compared with the symmetric structure.

same *y* direction (Fig. 12d). We restricted ourselves to possible distortions in the doubled unit cell. In all cases the short Sb–Sb distances were made 3.0 Å and the long ones 3.5 Å.

Our results show that indeed the sliding motion first studied is the most favorable one energetically. The pairing distortion is the least favored among the distortions that we considered. When all central Sb9 atoms move up in the *y* direction, one is left effectively with a kinked Sb chain on the one side and isolated Sb atoms on the other side. This deformation is comparable energetically to the structure produced by the up-and-down motion of the central Sb atoms. The latter motion creates Sb_3 "trimers" as in the real structure, but arranged differently in the chains. The relative instability of the last two structures (Figs. 12c, 12d) compared with the real strip from $La_{12}Mn_2Sb_{30}$, is not very great, indicating the possibility of their realization in other compounds. An analog of the distortion of Fig. 12c is found for the Sb_4 strips (instead of Sb_3) in the β-$ZrSb_2$ structure (12).

PUTTING THE Sb SUBSTRUCTURES TOGETHER

We have discussed in detail the electronic structure of the three-dimensional Sb_{20}^{16-} network and the one-dimensional Sb_3^{5-} strips. The third Sb substructure is the simplest by far; it consists of one-dimensional chains with a distance of 4.3 Å between the Sb6 atoms. The Sb6 atoms are essentially noninteracting at such a large distance. We might mention here that there exist rare earth metal antimony phases with linear Sb chains that do interact (7, 21), but this is not the case in the structure we study.

The three Sb substructures are effectively isolated from each other in the crystal of $La_{12}Mn_2Sb_{30}$ and there are no significant interactions between them. We assigned a $16-$ charge to the Sb_{20} network, a $10-$ charge to the Sb_6 strips, and a $12-$ charge for isolated Sb_4, which adds up to $38-$. The actual charge of the Sb_{30} substructure is $40-$, determined by a "Zintl count" from the charges on La and Mn. This small electron excess moves up the Fermi level slightly. For Sb_{30}^{40-} in the composite Sb sublattice, the Fermi level was calculated at -5.26 eV.

The question is which antimony sublattice is reduced? All bands of the isolated Sb6 atoms (Sb^{3-}) are already completely filled at a Fermi energy of -10.4 eV. For the Sb_3^{5-} strips, the lowest point of the empty bands 11 and 12 is at a rather high -4.25 eV (see Fig. 10a). Therefore these bands remain unfilled for the Fermi level of -5.26 eV in Sb_{30}^{40-} and our analysis of the second-order Jahn–Teller distortion in the strips will apply in the three-dimensional lattice. The Fermi level for the individual 3D Sb_{20}^{16-} network was found at -5.91 eV. It is this network that is probably reduced by addition of two extra electrons to the Sb substructure. We pointed out earlier that the Fermi level for 3D Sb_{20}^{16-} passes through the antibonding intrasheet but mainly nonbonding intersheet (Sb8–Sb8) states. As a consequence, the two-electron reduction of this network diminishes the Sb–Sb intra-

sheet overlap populations by 13%, while the intersheet overlap populations are reduced only by 1.5%.

INTERACTION OF Mn ATOMS WITH THE Sb_{30} SUBLATTICE

Our next step is the insertion of two Mn atoms into the unit cell of the Sb_{30}. In the language of molecular inorganic chemistry, we can imagine that the 3D Sb_{20}, the 1D Sb_3, and the 0D Sb substructures act as separate ligands in the subsequent interaction with Mn and La. The Mn sites were reported to be half-occupied; we choose the Mn sites in such a way that all the "on top" positions in structure **1** are occupied and all the "on bottom" positions are empty. The Mn atoms in the crystal structure of $La_{12}Mn_2Sb_{30}$ are far apart from each other and the particular choice of the Mn sites did not alter the results of the calculations. The local environment of Mn in the crystal structure is shown in Fig. 13. That local coordination of Mn may be described roughly as a distorted bicapped tetrahedron of Sb atoms. The orbital pattern in that unusual coordination geometry was discussed by one of us earlier (29, 30).

We assign an $8-$ charge to molecular $MnSb_6$ for the following reasons. Mn is assumed to be $2+$, as argued at the outset of the paper. An octet then is completed around each antimony ligand, leading to a $3-$ charge on each of the "isolated" Sb7 atoms and a $1-$ charge on Sb5 and Sb8 (**12**). The reason for the $1-$ charge is that Sb5 and Sb8 are part of a (kinked) square net; they are bonded to each other. As **12** shows we are modeling the four Sb5 and Sb8 ligands as an Sb_4^{4-} ring. The important bond distances and angles are given in Fig. 13; the Mn coordination sphere is quite irregular both in angles and in distances to the ligating antimony atoms.

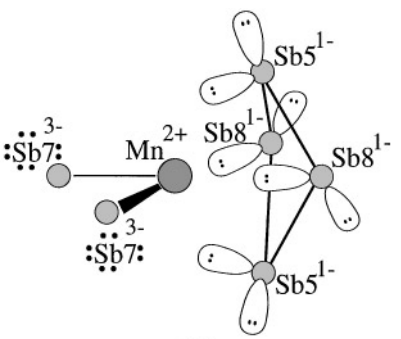

12

There are several ways to approach the Mn bonding in this model. The way we have found simplest is to build up the final geometry by interaction of a d^5 $MnSb_2^{4-}$ fragment with a puckered Sb_4^{4-} ring, which in turn is constructed from a square-planar ring. This assembly is indicated schematically in **13**. The coordinate system in the composite molecule is chosen in such a way (Fig. 13) that the x axis passes inbetween the Mn–Sb equatorial bonds.

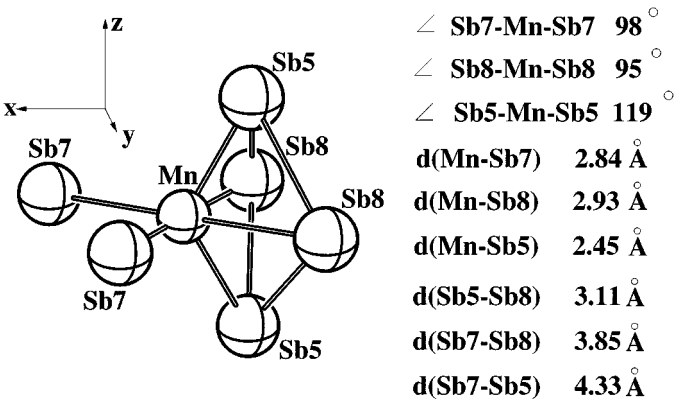

FIG. 13. Local environment of Mn in $La_{12}Mn_2Sb_{30}$.

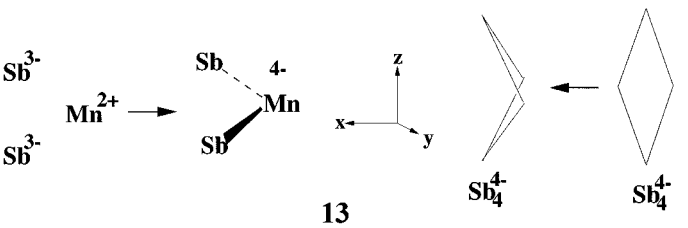

13

The actual interaction diagram is given in Fig. 14. The Sb_4^{4-} orbitals differ little from those of the square-planar ring; essential to the interaction is the all-filled cyclobutadienoid "π" set (one below two below one) of orbitals 7, 10, 11, and 12 of this fragment (Fig. 15). The $MnSb_2^{4-}$ orbitals are those typical of an ML_2 fragment (31). In the energy window chosen there is present a four below one pattern of d orbitals followed by a higher-lying hybrid of mainly sp_x character (Fig. 14, left).

Two of the d-block orbitals (d_{yz} and $d_{x^2-y^2}$) do not interact much with Sb_4^{4-} orbitals. The interaction of d_{xz} with one of the middle orbitals of the ring π orbitals (No. 11, Fig. 15) is excellent, but the resulting MO does not rise so high because of secondary interaction with a metal p_z above the energy window shown (32).

The other two orbitals, d_{z^2} and d_{xy}, are destabilized by effective interactions with Sb_4^{4-} orbitals. The net result is two-below-one-below-two pattern in the $MnSb_6^{8-}$ d block. The final shape of orbitals is shown in Fig. 16. The only atypical finding is substantial admixture of an Sb_4^{4-} fragment σ^* orbital into the d_{xy}; the symmetry-allowed mixing of the corresponding ring π orbital (No. 10 in Fig. 15) is hampered by poor overlap due to the Sb_4 ring puckering.

In the $MnSb_6^{8-}$ model the Mn is formally $2+$. However, our calculations actually yield a charge of -2.02 on the Mn. This is the result of substantial Mn–Sb mixing of all Mn d-block orbitals into lower Sb levels. This mixing, in

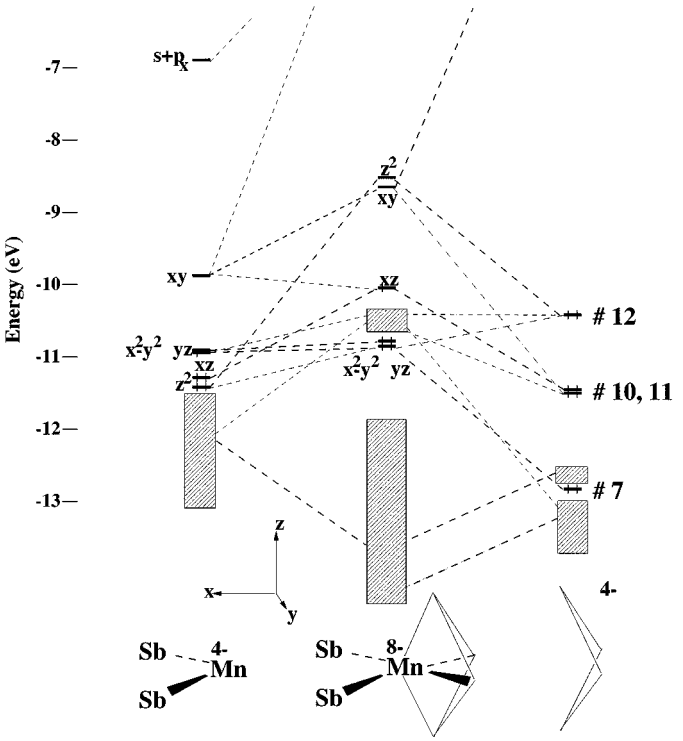

FIG. 14. Interaction diagram between $MnSb_2$ and Sb_4 fragments. Only relevant orbitals are shown; the rectangular blocks indicate orbitals not discussed, mainly centered on the antimony atoms.

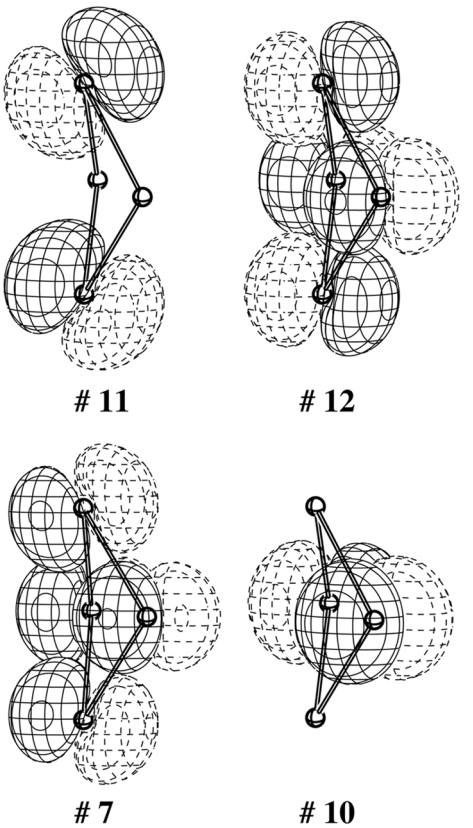

FIG. 15. π'' set of orbitals of the Sb_4^{4-} fragment.

turn, may be traced back to the near equality of Mn 3*d* and Sb 5*p* H_{ii}'s. Nevertheless, five electrons reside in predominantly Mn 3*d* orbitals, which is why we describe the molecule still as an Mn d^5 species. However, our extended Hückel calculations cannot deal with the high-spin state adequately, nor give its energy well relative to a low-spin configuration. For that one needs an accurate description of electron–electron repulsion and exchange.

Having completed the analysis of the molecular model, we move to the fully extended $Mn_2Sb_{30}^{36-}$. The contributions of the Mn *d* block to the total DOS of the molecular $MnSb_6^{8-}$ complex and the extended $(Mn_2Sb_{30})^{36-}$ substructure are quite comparable. This similarity argues in favor of a significant localization of Mn–Sb bonds in the extended substructure. The same conclusion emerges from a comparison of the Mn–Sb COOPs for the molecular model and the extended substructure (not shown here). The localized nature of Mn bonding in the extended structure is consistent with the existence of the magnetic moment on Mn.

We compute a -3.3 charge on Mn for the Mn_2Sb_{30} substructure and a -2.5 charge on Mn in the full crystal structure of $La_{12}Mn_2Sb_{30}$. The Mn *d* block is nearly filled, and this is inconsistent with the magnetic moment evidence. If electron–electron repulsion had been explicitly taken into account in the calculations, the double occupation of Mn *d* orbitals might have been prevented. Since in reality the Mn states are less filled than our calculation indicates, this means that there has to be an effective reduction by a few electrons of the rest of the atoms in $La_{12}Mn_2Sb_{30}$. This artifact of the extended Hückel calculations should not cause a major problem, taking into account the large number of electrons (200) in the unit cell.

Finally, we may note that the introduction of Mn into the Sb_{30} network is a very small perturbation for that sublattice. All Sb contributions to the total DOS of Mn_2Sb_{30} as well as different Sb–Sb COOP curves remain virtually unchanged on addition of the Mn ions. This result is a consequence of the small Mn : Sb ratio and the strong localization of the bonds in the structure.

INCLUSION OF La IN THE Mn_3Sb_{30} SUBSTRUCTURE

The last step in the assembly of $La_{12}Mn_2Sb_{30}$ is the addition of La atoms to the Mn_2Sb_{30} subnetwork. We describe this last perturbation very qualitatively, because the parameters for La that we use are not very well defined, and *f* orbitals are not explicitly included.

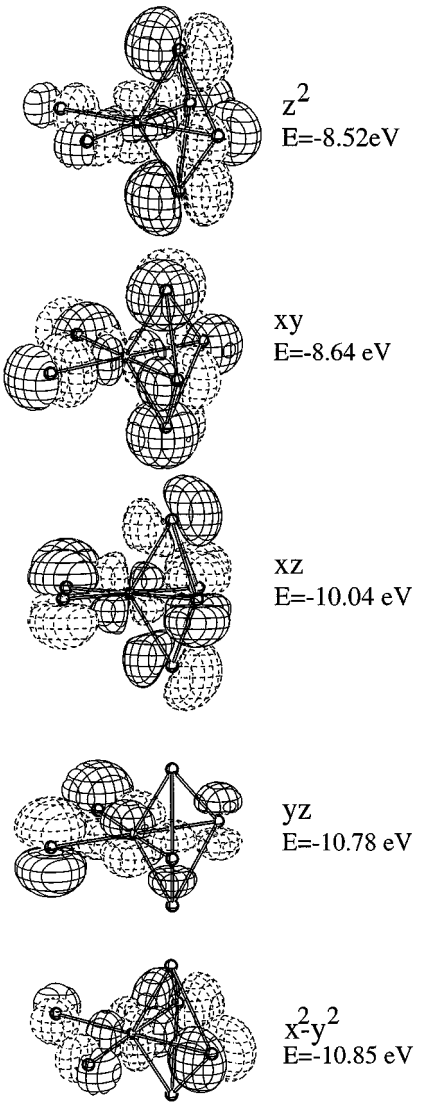

FIG. 16. Mn *d*-block orbitals of the $MnSb_6^{8-}$ model.

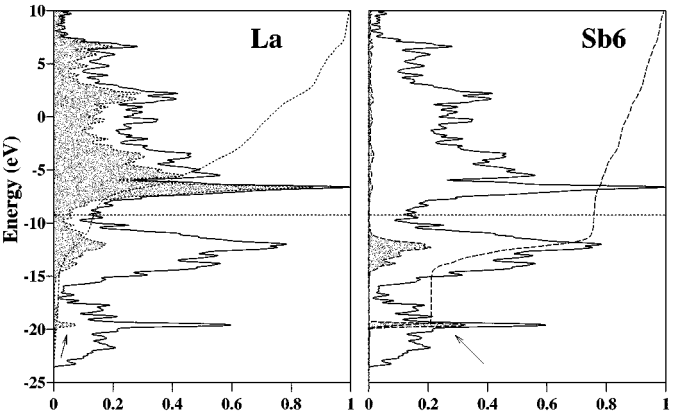

FIG. 17. Contributions of La and Sb6 atoms to the total DOS of $La_{12}Mn_2Sb_{30}$.

The structure itself suggests that the inclusion of La atoms into the Mn_2Sb_{30} substructure might be a significant perturbation; there are large numbers of relatively short La-to-other atoms bonds in $La_{12}Mn_2Sb_{30}$. Indeed in our calculations a substantial number of La levels are occupied; the computed charges on La atoms are $+0.55$, quite far from the formal $3+$. Thus, the La atoms not only donate their electrons, but also interact significantly with the neighboring atoms. The La and Sb contributions to the total DOS of $La_{12}Mn_2Sb_{30}$ are shown in Fig. 17. The interaction with La lowers the Sb levels, especially near the Fermi level (the Fermi level itself is somewhat lowered). Another consequence of the interaction of La with other atoms is a broadening of corresponding contributions to the total DOS of $La_{12}Mn_2\ Sb_{30}$. For example, the narrow bands of the originally noninteracting zero-dimensional Sb6 atoms in Mn_2Sb_{30} are significantly broadened and somewhat lowered (see Sb6 contribution to the total DOS of $La_{12}Mn_2Sb_{30}$, Fig. 17, right). The interaction of La with Sb6 is clearly illustrated by the lowest peak of the La contribution to the total DOS of $La_{12}Mn_2Sb_{30}$, a peak that is in the same region as the Sb6 *s* contribution to the total DOS (these peaks are indicated with arrows in Fig. 17). The remaining small part of that sharp peak in the total DOS is contributed by other Sb atoms.

The total DOS at the Fermi level is composed mainly of the La and the 3D Sb_{20} sublattices. For the latter sublattice the main contribution comes from slightly antibonding and nonbonding intrasheet bands. This results in the potential of the 3D Sb_{20} subnetwork to undergo redox reactions without too much energy change. Mar and co-workers suggested the role of Sb substructures as electronic sinks, based on their experimental data (7).

The position of the Fermi level (in a region of some DOS) is consistent with the metallic properties of the alloy.

The various Sb–Sb COOP curves in the Mn_2Sb_{30} substructure are not strongly affected by the inclusion of La. This finding supports the idea of the strong localization of the bonds in the crystal structure of $La_{12}Mn_2Sb_{30}$.

We conclude this section by a description of the charges on La and Sb in $La_{12}Mn_2Sb_{30}$. An average positive charge of 0.55 was found on the La atoms. These atoms are electropositive, yet involved in bonding. The zero-dimensional Sb6 atoms were most negatively charged (-1.07), also in agreement with the electronegativity and Zintl considerations. The Mn atom charges were discussed above. The central Sb atoms in the strips carry less negative charge (-0.07) than the side Sb atoms (an average of -0.49). Only half of the Mn sites are occupied in $La_{12}Mn_2Sb_{30}$ (see **1**) therefore, in the assumed ordered structure the side Sb atoms in the strips are not equivalent to each other throughout

the crystal. The side Sb atoms connected to Mn are less negative (-0.22) than those neighboring the Mn voids (-0.75). The lone pairs on the Sb atoms near the voids are not shared with Mn, which rationalizes their higher negative charge. A related effect was observed for Sb5 (0.02 and 0.25) and Sb8 (0.55 and 0.71) atoms in the kinked sheets. The Sb4 atoms in the kinked sheets are located further away from the Mn sites and the difference between the charges of nonequivalent atoms is much smaller (0.10 and 0.13).

CONCLUSIONS

We carried out a sequence of geometrical perturbations of simple building blocks to assemble the full structure of $La_{12}Mn_2Sb_{30}$. First, the band structure of a square sheet of Sb was analyzed in detail. Kinking of the sheet at every fifth diagonal line produces directional orbitals at the corner Sb atoms. These orbitals are mainly responsible for the interaction between the sheets when stacked into a three-dimensional network. We provided what we believe are convincing arguments for strong localization of intersheet bonds in the 3D Sb_{20} substructure.

Another substructure in $La_{12}Mn_2Sb_{30}$ is the one-dimensional strip of Sb_3 (Sb_6 in the doubled cell). A possible sliding motion of the central atoms could produce more symmetrical strips. The band structure and the crystal orbitals of a symmetrical 1D Sb_3 strip were built up. A distortion in which the mirror plane perpendicular to the strip axis is lost leads to mixing between the highest occupied and lowest unoccupied crystal bands, which might be called a second-order Peierls distortion. The stabilization (1.25 eV) of the crystal band **10** due to the sliding motion of the central Sb atoms is mainly responsible for the overall stabilization (1.32 eV) of the distorted (real) strip. The last Sb substructure consists of chains of noninteracting Sb^{3-} atoms.

We then put the three Sb substructures together. A calculation on the 3D Sb_{30}^{40-} sublattice confirms the absence of interactions between the Sb_{20}, the Sb_6, and the Sb_4 substructures. The inclusion of Mn^{2+} atoms into Sb_{30}^{40-} does not alter the Sb–Sb COOP curves in the latter substructure, indicating once more the localized character of bonding in the Sb network. We analyzed in detail the Mn *d*-block splitting. The excessive -2.49 charge on Mn calculated for the full $La_{12}Mn_2Sb_{30}$ structure is a consequence of the absence of electron–electron repulsion and exchange in the extended Hückel method.

The contributions of Sb atoms to the total DOS of $La_{12}Mn_2Sb_{30}$ are diminished due to interaction with La. The Sb–Sb COOP curves remain virtually unchanged, confirming once more the strong localization of the bonds in the structure. The position of the Fermi level for the full crystal structure of $La_{12}Mn_2Sb_{30}$ is in accord with the conducting character of $La_{12}Mn_2Sb_{30}$.

TABLE 1
Extended Hückel parameters[a]

Atom	Orbital	H_{ii} (eV)	ζ_1	c_1	ζ_2	c_2	Ref.
Sb	5*s*	-18.8	2.323				(34)
	5*p*	-11.7	1.999				
Mn	4*s*	-7.5	1.80				(35)
	4*p*	-3.8	1.80				
	3*d*	-8.7	5.15	0.5140	1.70	0.6930	
La	6*s*	-7.67	2.14				(36)
	6*p*	-5.01	2.08				
	5*d*	-8.21	3.78	0.7765	1.381	0.4586	

[a] The ζ's are the exponents of the Slater orbital basis set, the c_i's are the coefficients in a double-ζ expansion.

The extension of our analysis of bonding in $La_{12}Mn_2Sb_{30}$ to other members of the RE_6MSb_{15} family is straightforward. Since the *d* blocks of Cu and Zn are well below the ntimony *p* block, we expect both metals to approach a d^{10} configuration, Cu^{1+}, Zn^{2+}. That places formally 38 and 40 electrons, respectively, into the Sb sublattice. If we examine the states around the Fermi level, they are pretty much Sb–Sb nonbonding, so that the main-group bonding would not be affected by this small variation in electron count. The same states are Mn–Sb antibonding, so if a rigid band model is assumed the 40 electron phases would have a weaker M–Sb bond.

The retrotheoretical/building up analysis, using the tools of the perturbation theory coupled with molecular orbital calculations, is shown to be a powerful tool for understanding the seemingly complicated bonding in the three-dimensional network of $La_{12}Mn_2Sb_{30}$. Some of the antimony substructures studied are common in other rare earth metal antimony phases, and we will study the bonding patterns in this intriguing family of compounds in contributions to come.

APPENDIX I: COMPUTATIONAL DETAILS

All calculations were performed with the help of Yet Another extended Hückel Molecular Orbital Package (YAeHMOP), a program developed in our group by G. Landrum (33). The standard atomic parameters were used for Sb, Mn, and La. The parameters are listed in Table 1 with the corresponding references.

ACKNOWLEDGMENTS

We thank Grigori Vajenine and Norman Goldberg for helpful discussions. We are grateful to the National Science Foundation for its support of this work by Research Grant CHE 94-08455.

REFERENCES

1. O. Sologub, M. Vybornov, P. Rogl, K. Hiebl, G. Cordier, and P. Woll, *J. Solid State Chem.* **122,** 262 (1996).
2. B. R. Wand and H. Steinfink, *Inorg. Chem.* **6,** 1685 (1967).
3. O. Sologub, H. Noël, A. Leithe-Jasper, and P. Rogl, *J. Solid State Chem.* **115,** 441 (1995).
4. O. Sologub, K. Hiebl, P. Rogl, H. Noël, and O. Bodak, *J. Alloys Compds.* **210,** 153 (1994).
5. A. Leithe-Jasper and P. Rogl, *J. Alloys Compds.* **203,** 133 (1994).
6. G. Cordier, H. Schäfer, and P. Woll, *Z. Naturforsch. B Chem. Sci.* **40,** 1097 (1985).
7. M. J. Ferguson, R. W. Hushagen, and A. Mar, *J. Alloys Compds.* **249,** 191 (1997).
8. M. Brylak and W. Jeitschko, *Z. Naturforsch. B Chem. Sci.* **50,** 899 (1995).
9. M. Brylak, M. H. Möller, and W. Jeitschko, *J. Solid State Chem.* **115,** 305 (1995).
10. W. K. Hofmann and W. Jeitschko, *J. Less-Common Met.* **138,** 313 (1988).
11. A. J. Ashe III, E. G. Ludwig Junior, J. Oleksyszyn, and J. C. Huffman, *Organometallics* **3,** 337 (1984).
12. E. Garcia and J. D. Corbett, *J. Solid State Chem.* **73,** 452 (1988).
13. R. Hoffmann, *J. Chem. Phys.* **39,** 1397 (1963).
14. R. Hoffmann, *J. Chem. Phys.* **40,** 2745 (1964).
15. R. Hoffmann, *J. Chem. Phys.* **40,** 2474 (1964).
16. W. Tremel and R. Hoffmann, *J. Am. Chem. Soc.* **109,** 124 (1987).
17. R. E. Peierls, "Quantum Theory of Solids," Oxford Univ. Press, London, 1955.
18. A. Rehr and S. M. Kauzlarich, *J. Alloys Compds.* **207,** 424 (1994).
19. T. Albright, J. Burdett, and M.-H. Whangbo, "Orbital Interactions in Chemistry," Chap. 14, Wiley, New York, 1985.
20. Note that the geometry here implies a square-planar carbon environment, hardly typical. The formally 4-C also has two lone pairs. What actually happens in the Sb^{-1} sheet will be sorted out below, in examining the detailed calculation.
21. M. Brylak and W. Jeitschko, *Z. Naturforsch. B Chem. Sci.* **49,** 747 (1994).
22. Concerning the charge balance, we suggest in the text the oxidation of the Sb_{30}^{40-} network to Sb_{30}^{38-}, based on La^{3+} and Mn^{2+}. A reviewer suggests that O. Sologub *et al.* did not refine the Mn occupation factor τ, but fixed it at 0.5. The reviewer then wonders if the real composition might be $La_{12}Mn_{2+x}Sb_{30}$. Ln–transition metal–ion (or chalcogen) compounds sometimes are nonstoichiometric at the transition metal site.
23. R. S. Mulliken, *J. Chem. Phys.* **23,** 2343 (1955).
24. R. Hoffmann, "A Chemist's View of Bonding in Extended Structures," p. 16, VCH, New York, 1988.
25. T. Hughbanks and R. Hoffmann, *J. Am. Chem. Soc.* **105,** 3528 (1983).
26. T. Albright, J. Burdett, and M.-H. Whangbo, "Orbital Interactions in Chemistry," Chap. 9, Wiley, New York, 1985.
27. C. Zheng and R. Hoffmann, *J. Phys. Chem.* **89,** 4175 (1985).
28. For a recent treatment of the second-order Jahn–Teller effect in solids, see M. A. Pell, G. V. M. Vajenine, and J. A. Ibers, *J. Am. Chem. Soc.* **119,** 5186 (1997).
29. R. Hoffmann, J. M. Howell, and A. R. Rossi, *J. Am. Chem. Soc.* **98,** 2484 (1976).
30. P. Kubáček and R. Hoffmann, *J. Am. Chem. Soc.* **103,** 4320 (1981).
31. T. Albright, J. Burdett, and M.-H. Whangbo, "Orbital Interactions in Chemistry," Chap. 19, Wiley, New York, 1985.
32. Fragmentation of $CpML_2$ into Cp and ML_2 is discussed in detail in T. Albright, J. Burdett, and M.-H. Whangbo, "Orbital Interactions in Chemistry," p. 370, Wiley, New York, 1985.
33. G. A. Landrum, http://overlap.chem.cornell.edu:8080/yaehmop.html (1995).
34. T. Hughbanks, R. Hoffmann, M.-H. Whangbo, K. R. Stewart, O. E. Eisenstein, and E. Canadell, *J. Am. Chem. Soc.* **104,** 3876 (1982).
35. M. Elian and R. Hoffmann, *Inorg. Chem.* **14,** 1058 (1975).
36. C. Zheng and R. Hoffmann, *Inorg. Chem.* **28,** 1074 (1989).